29th Congress of the International Council
of the Aeronautical Sciences
St. Petersburg, Russia; September 7–12, 2014

AIRCRAFT ICING IN FLIGHT: EFFECTS OF IMPACT OF SUPERCOOLED LARGE DROPLETS

Ellen Norde*, **Jacco M. Hospers***, **Edwin van der Weide***, **Harry W.M. Hoeijmakers***
***University of Twente, Enschede, The Netherlands**

Keywords: *Icing, Multi-Phase, Splashing, SLD, Eulerian*

Abstract

In this study a computational method is presented which simulates the presence of a liquid layer on an airfoil and its effect on splashing of Supercooled Large Droplets (SLD). The thin liquid film is expected to have a significant influence on the impact behaviour of SLD. It will arise when the impacting droplets freeze only partially and leave behind a layer of runback water on top of the ice layer. The liquid film is modelled using the wall shear stress and by assuming a linear velocity profile within the water layer. The shear stress is calculated by coupling an integral boundary-layer method to a potential flow method.

The SLD splashing model is extended with a deposition model that accounts for impact on a liquid film and includes the solidification time of the droplets. This solidification time is obtained using multiple approaches which are based on either planar solidification or dendritic solidification. Planar solidification is controlled by diffusion and based on the Stefan problem for heat conduction. Dendritic solidification is more rapid and mostly governed by kinetics.

The comparison of the catching efficiency with experimental results for a NACA-23012 airfoil shows a significant improvement employing the new deposition model. Also, good agreement is found with the experimental results for the ice accretion on a NACA-0012 airfoil.

1 Introduction

Supercooled Large Droplets (SLD) are water droplets with a diameter larger than 40 microns. In clouds they can form through melting of snow or coalescence of smaller droplets under influence of wind shear. After the fatal crash of an ATR-72 commuter aircraft near Roselawn, Indiana in 1994 [1] SLD were recognized as extremely hazardous. This type of icing can occur at different locations on the aircraft and is faster and more unpredictable compared to icing by smaller droplets. This year the FAA will present the final regulations for SLD icing conditions specified in appendix O of 14 CFR part 25 [2].

In the past years much research has been carried out considering in-flight SLD icing. The European Union sponsored project EXTICE (EXTreme ICing Environment) [3], that ran from 2008 until 2012, included droplet impact experiments, icing experiments and numerical simulations with improved SLD-specific models. In this framework the University of Twente developed a computational method capable of predicting ice accretion due to multi-disperse droplet distributions of splashing and rebounding SLD based on an Eulerian trajectory model.

In the present paper the computation of a thin liquid film and its effect on splashing SLD via an improved deposition model will be described with which the existing computational method has been expanded. The new deposition model has been proposed by Li et al. [4] from Darmstadt University of Technology and takes the solidification time of the liquid layer into ac-

count. Numerical results are compared with data from experiments by Papadakis et al. [5] for a NACA-23012 airfoil and with data obtained by DGA Aero-engine Testing from experiments for a NACA-0012 airfoil. Both Darmstadt University of Technology and DGA Aero-engine Testing were partners in the EXTICE project.

2   SLD Physics

Because of the relatively large size of SLD, their impact behaviour needs to be taken into account in order to model the physics of SLD accurately. The phenomena occurring may include: splashing, rebound, breakup, deformation or a combination of these. In case of splashing the droplets will breakup into smaller secondary particles, as is shown in Fig. 1, while the droplet will bounce from the surface completely in case of a rebound event. Before SLD hit the surface they can either deform or breakup into smaller droplets. In the current method only splashing and rebound are implemented and pre-impact breakup and deformation are ignored. For the SLD splashing model a mass-loss coefficient by Honsek et al. [6] is used, while the number of secondary droplets and their velocity distribution have been obtained from Trujillo et al. [7]. The rebound model is based on work from Bai and Gosman [8].

The computational method solves the droplet distribution sequentially, that is from the bin with the largest droplets to the bin with the smallest droplets. This implies that coalescence is ignored. The secondary droplets that are created after a splashing or rebound event are added to the bin with droplets that have a diameter corresponding to the diameter of the secondary droplets. If splashing or rebound occurs, in elements next to the surface of the airfoil, the local
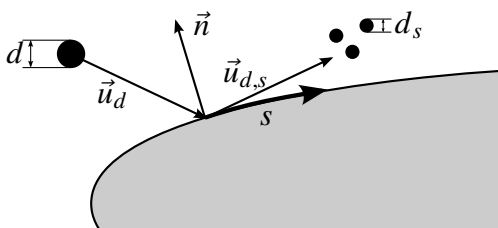

Fig. 1 : Splashing variables.

re-injected mass and momentum are imposed via boundary conditions.

3   Numerical Method

The numerical method that forms the starting point for this research has been developed by J.M. Hospers [9, 10]. This method uses an Eulerian droplet tracking approach in combination with a Finite Volume Method for unstructured grids. A droplet size distribution divided into a number of bins with a certain range of droplet size and a two-dimensional potential flow field solution will be provided as input for the calculation of the droplet trajectories. In the trajectory calculation it is assumed that the droplets form a dilute distribution and that they can be treated using one-way coupling, i.e. droplets have a negligible effect on the flow field. With the Eulerian mass and momentum equations, Eq. (1) and (2), the droplet density ρ_d and the droplet velocity $\vec{u}_d$ are calculated on the computational grid.

$$\frac{\partial \rho_d}{\partial t} + \vec{\nabla} \cdot (\rho_d \vec{u}_d) = 0, \tag{1}$$

$$\frac{\partial \rho_d \vec{u}_d}{\partial t} + \vec{\nabla} \cdot ((\rho_d \vec{u}_d)\,\vec{u}_d) = \rho_d \vec{f}_D$$
$$+ \rho_d \left(1 - \frac{\rho_a}{\rho_w}\right)\vec{g}. \tag{2}$$

Here, $\vec{f}_D$ is the drag force per unit mass, $\vec{g}$ the gravitational acceleration, ρ_a the density of air and ρ_w the density of water. The source terms in the momentum equation are the drag, gravity and buoyancy force acting on the droplet. The virtual mass force, Basset history force and other force terms are neglected [11].

Solving the Eulerian equations in combination with the SLD splashing and rebound model will result in a water catching efficiency distribution β along the airfoil. This distribution serves as input for the ice accretion method. This method is based on the Messinger model [12] in which the heat and mass balance for the flow of water along the surface are solved to calculate the rate of increase of the thickness of the ice layer. A detailed explanation can be found in Jacobs et al. [13].
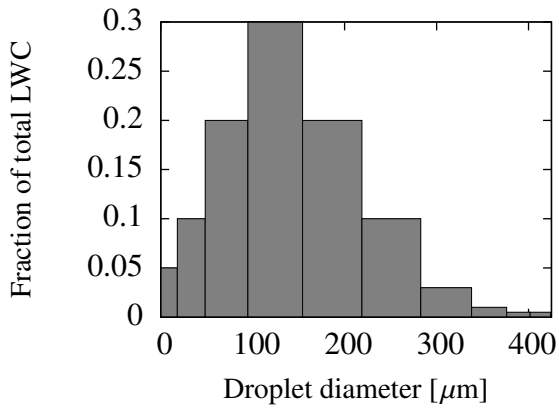
Fig. 2 : Papadakis' test case: mono-modal droplet distribution, 154 μm MVD, 10 bins. Data from Papadakis et al. [5]
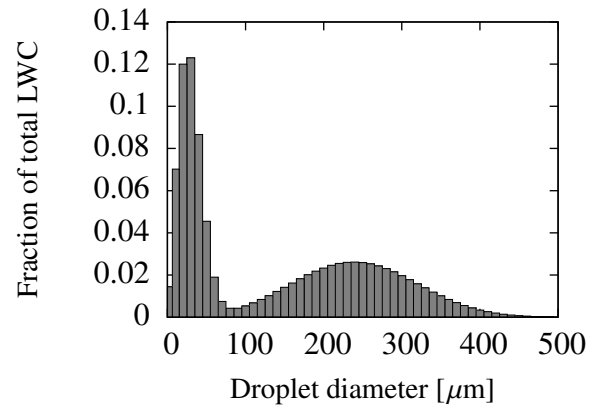

Fig. 3 : DGA test case: bi-modal droplet distribution, 104 μm MVD, 50 bins.

In summary, the SLD icing prediction methodology consists of four steps:

1. Flow simulation;

2. Eulerian droplet tracking with specific treatment of SLD resulting in the distribution of the water catching efficiency along the airfoil;

3. Computation of the rate of ice accretion from Messinger's thermodynamic model;

4. Calculation of the new ice shape.

4   Test cases

The results of the new deposition model will be compared with experimental results from two test cases. In the first test case the catching efficiency will be compared with results from experiments by Papadakis et al. [5]. These experiments have been conducted in the Icing Research Tunnel of NASA Glenn Research Center. It concerns a 36-inch NACA-23012 airfoil placed at an angle of attack of 2.5° in a droplet flow with a free-stream velocity of 78.23 m/s, a temperature of 299 K and an ambient pressure of 101330 Pa. Catching efficiency data has been obtained for both clean and iced configurations of the airfoil. The droplet cloud consisted of a 10-bin mono-modal droplet distribution (see Fig. 2) with a median volumetric diameter (MVD) of 154 μm and a liquid water

content (LWC) of 1.44 g/m^3. This test case is referred to as Papadakis test case A. In Papadakis test case B all conditions are the same except for the air temperature. This temperature is lowered to 268.15 K and the icing time is set to 600 s to analyse the changes in the ice shape obtained with the numerical method. There are, however, no experimental results available for this lower temperature.

In the second test case the ice shape will be compared with experiments from DGA Aero-engine Testing. During the EXTICE 2D test campaign 22 icing wind-tunnel tests have been performed on a steel-made NACA-0012 airfoil of 800 mm chord. Run 18 is chosen for comparison in which data was gathered for an airfoil at a 2° angle of attack in a flow field with the following conditions: Mach 0.5, altitude 4000 m, temperature -10°C, icing time 450 s. The droplet diameter distribution is shown in Fig. 3. It is a 50-bin bi-modal distribution of MVD 104 μm and LWC 0.3 g/m^3.

For both test cases a computational grid is needed as input for the Eulerian droplet trajectory method. The meshes for the NACA-23012 (see Fig. 4) and the NACA-0012 airfoils consist of 18300 and 17952 triangular elements, respectively. These finite-element meshes are then converted to edge-based finite-volume meshes employed by the numerical method.
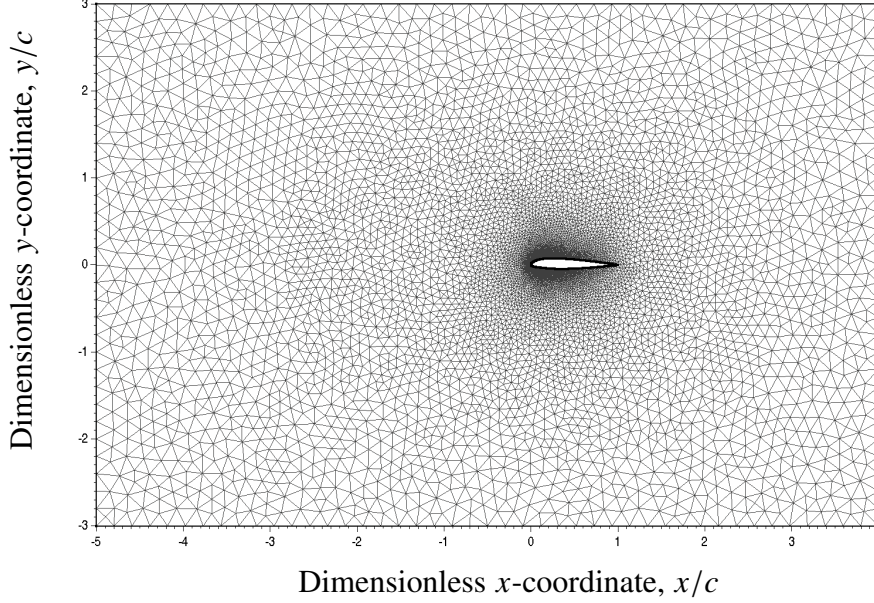
Fig. 4 : Mesh around a NACA-23012 airfoil with 18300 triangular elements.

5 Liquid film: model and results

The presence and thickness of a liquid layer can have a significant effect on the splashing behaviour of droplets as has already been investigated by Tropea and Marengo [14] and is shown in experiments of Wang and Chen [15]. A liquid film will arise when the impacting SLD freeze only partially resulting in a water layer on top of the ice layer, shown schematically in Fig. 5. In this schematic u_w is the velocity of the water layer. It is assumed that the velocity profile in the layer is linear and that there is no slip at the ice-water interface. This leads to the following expression for u_w:

$$u_w(y) = U_w \frac{y}{h_w}, \qquad \text{where} \quad U_w = h_w \frac{\tau_w}{\mu_w}, \quad (3)$$

with U_w the velocity at the air-water interface, h_w the water layer height and μ_w the dynamic viscosity of water. τ_w is the shear stress in the water layer imposed by the airflow over the water layer:

$$\tau_w = \mu_w \left(\frac{\partial u_w}{\partial y} \right)_{y=h_w^-} = \mu_a \left(\frac{\partial u_a}{\partial y} \right)_{h=h_w^+}, \qquad (4)$$

with μ_a the viscosity of air and $u_a(y)$ the velocity profile in the air. In the Messinger model the mass flow rate of the inflowing liquid water per

unit length in spanwise direction is calculated by setting it equal to the impinging water mass flow rate minus the sum of the mass flow rates due to evaporation, splashing, ice mass and outflowing runback water. The height of the water layer can be obtained by expressing the inflowing mass flow rate in terms of water height h_w, water density ρ_w and the velocity of the liquid layer $u_w(y)$. Together with the expression in Eq. (3) this gives:

$$\dot{m}_{in} = \int_{h_w} \rho_w u_w(y) \mathrm{d}y = \frac{1}{2} \rho_w \frac{\tau_w}{\mu_w} h_w^2. \qquad (5)$$

The wall shear stress can be expressed in terms of the skin friction coefficient, which is calculated by coupling a turbulent boundary-layer method to the second-order panel method [16]. The laminar flow region is calculated with Thwaites' method (1949) [17], the turbulent flow region is computed with Head's entrainment method (1958) [18] and the criterion of Michel (1951) [19] is used to determine the location of transition from laminar to turbulent flow. This model is only used to calculate the wall shear stress in order to compute the liquid film. In the boundary-layer method the effect of the presence of the liquid film is not taken into account, i.e. it is assumed that the velocity in the liquid layer is very small compared to the velocity of the air over the water layer.
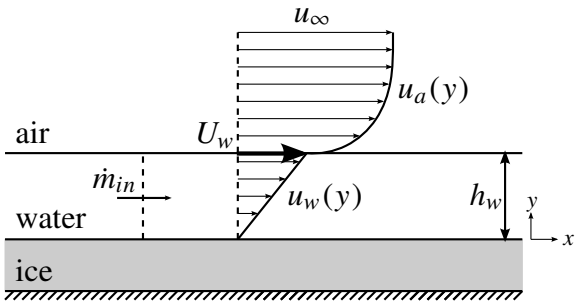
Fig. 5 : Boundary layer on top of liquid layer, note that drawing is not to scale as $U_w \ll u_\infty$.
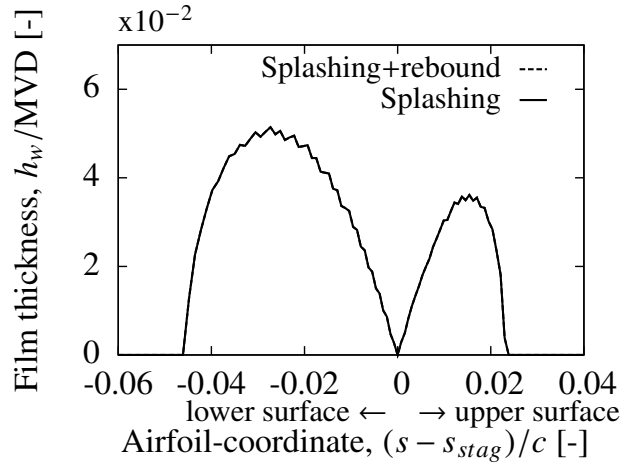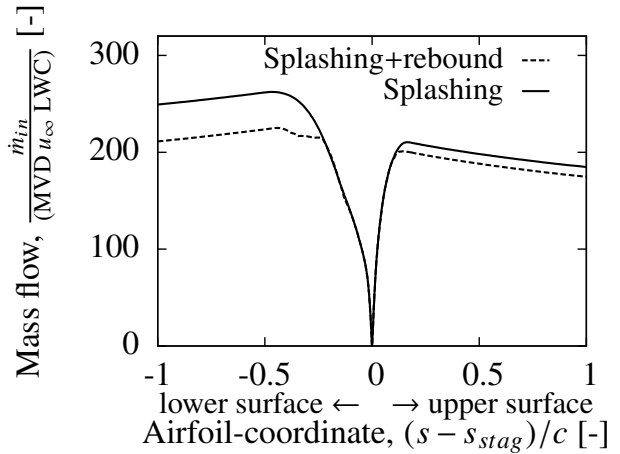

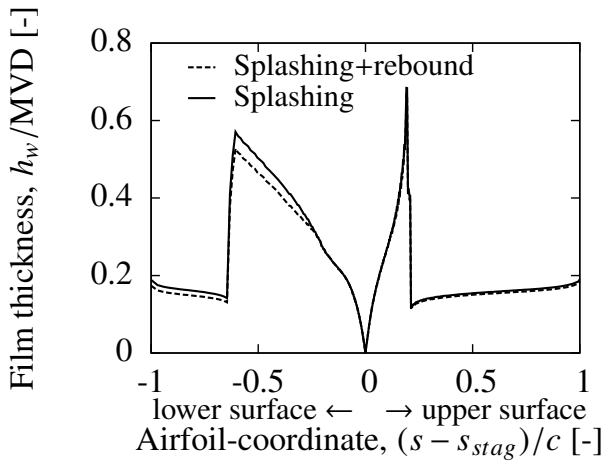Fig. 6 : Water film thickness, DGA test case.

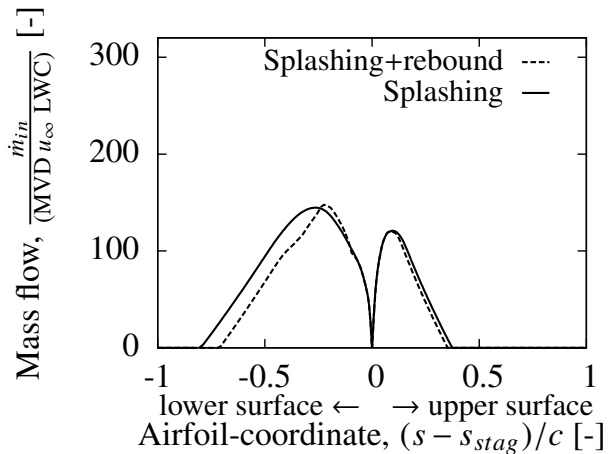Fig. 7 : Water film thickness (left) and mass flow (right) for Papadakis test case A ($T = 299$ K).
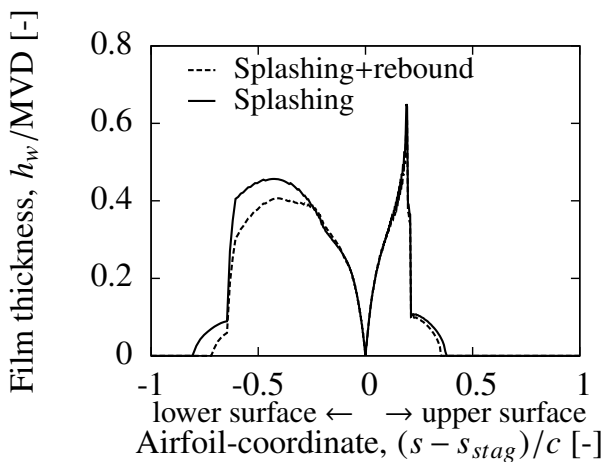

Fig. 8 : Water film thickness (left) and mass flow (right) for Papadakis test case B ($T = 268.15$ K).

5.1 Results

The liquid layers are computed for the two test cases introduced in section 4 and the results are shown in Fig. 6 to Fig. 8. In these and all further graphs the airfoil coordinates are scaled with the chord c of the airfoil. The liquid film thickness is made dimensionless with the MVD and the mass flow is scaled with the product of the MVD, the free-stream velocity and the LWC.

The results for the liquid film thickness computed for the DGA test case, see Fig. 6, show that there is a liquid layer of a few microns thickness around the stagnation point. The film thickness computed with the SLD splashing model matches exactly the film thickness computed with the combined SLD splashing and rebound model. Actually, this test case was chosen from the available 22 test cases because it showed the thickest liquid layer. This should imply that the new deposition models show an ice shape that differs from the ice shape computed using the original method as will be discussed further in section 9.

For Papadakis test case A ($T = 299$ K) the results for the liquid film thickness and the mass flow for the splashing model and for the combined splashing and rebound model are presented in Fig. 7. From the left graph in Fig. 7 it can be seen that a liquid layer is present on the whole airfoil surface, except at the stagnation point. Around the stagnation point the film height will increase due to the increase of the incoming mass flow $\dot{m}_{in}$, see the right graph of Fig. 7. The liquid film strongly reacts to changes in the skin friction coefficient. At the transition point from laminar to turbulent flow the film thickness abruptly decreases from about 80-90 μm to about 20-30 μm. Furthermore, h_w differs slightly for the SLD splashing model on the one hand, and for the combined SLD splashing and rebound model on the other hand. This is because $\dot{m}_{in}$ is slightly smaller when rebound is included.

When the air temperature is 268.15 K (Papadakis test case B), this results in a different liquid layer of which the results are shown in Fig. 8 for the film thickness (left) and the runback mass flow (right). At this lower temperature the film does not cover the whole airfoil surface because

it freezes on the surface before the trailing edge is reached. Still, the part of the airfoil contour covered by the film is large enough to be influenced by the boundary layer transition. Downstream of the transition point, the film height rapidly drops to zero because of the decreasing runback mass flow.

6 Deposition model

Li et al. [4, 20] developed a deposition model based on experimental results using a small-scale facility for single drop impact [3]. These experiments have been executed at droplet velocities ranging from 30 m/s to 60 m/s and for a droplet diameter of 150 μm. Two empirical mass-loss correlations have been obtained, one for impact on a dry substrate, Eq. 6, and one for spray impact on a liquid substrate, Eq. 7. If the splashing parameter or the dimensionless number has a subscript n, the normal velocity component is used to calculate these quantities.

$$\phi_{dry} = 0.25 \left[1 - \frac{1}{1 + \exp[(K_n - 8850)/1200]} \right], \tag{6}$$

$$\phi_{spray} = 0.5 - 0.616 \exp(-K/750.9), \\ (K > 156.6). \tag{7}$$

The relations depend on a critical Cossali splashing parameter K, which is defined as a function of the Ohnesorge and Weber number:

$$K = \text{Oh}^{-2/5}\text{We}. \tag{8}$$

The Weber number relates kinetic energy to the surface energy due to surface tension and the Ohnesorge number relates viscous forces to the square root of inertial forces and surface tension. This results in:

$$\text{Oh} = \frac{\mu_w}{\sqrt{\rho_w \sigma_w d}}, \quad \text{We} = \frac{\rho_w \vec{u}_d^2 d}{\sigma_w}. \tag{9}$$

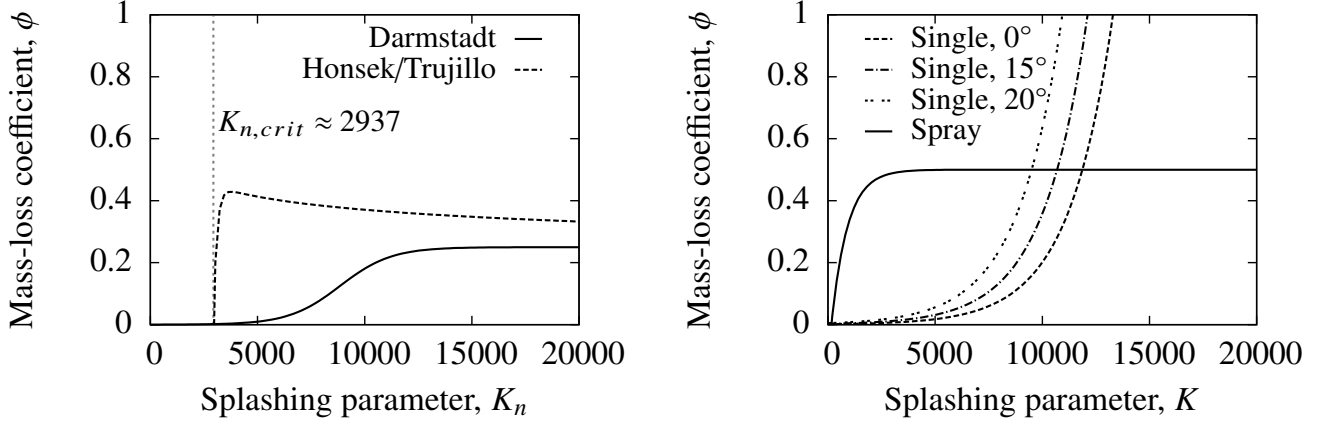For single drop impact onto a planar water surface the empirical relation developed by Okawa

Fig. 9 : Mass-loss coefficient for drop impact on a dry substrate (left) and on a liquid substrate (right).

et al. [21] is used:

$$\phi_{single,0} = 0.00156 \exp[0.000486K],$$
$$\text{if } 0° < \theta < 10° \text{ and } K > 2100,$$
$$\phi_{single} = \phi_{single,0} \exp[0.115(\theta - 10°)],$$
$$\text{if } 10° \leq \theta \leq 50° \text{ and } K > 2100, \quad (10)$$

where θ is the inclination angle in degrees between the velocity vector and the normal to the substrate. It is proposed to consider the spray impact relationship as an upper bound for deposition and to use the following minimum for the deposited mass on a liquid substrate:

$$\phi_{wet} = \min\left[\phi_{single}, \phi_{spray}\right]. \quad (11)$$

In the left graph of Fig. 9 the mass-loss coefficient for a dry substrate is plotted together with the original mass-loss coefficient used in the current method, i.e. the one defined by Honsek et al. [6] with a splashing parameter from Trujillo et al. [7]. The mass-loss coefficients for a liquid surface are shown in the right graph (Fig. 9). The relation for single drop impact is given for three different impact angles of $\theta = 0°, 15°$ and $20°$.

6.1   Surface condition

When a droplet touches the surface it produces a liquid splat that spreads outwards. A wetting parameter N_h is used to determine whether the surface is dry or wet. If N_h is smaller than one, the surface is assumed solid and if N_h is larger than one, the splat does not solidify fast enough and

the deposition model has to account for a liquid film. N_h depends on the volumetric flux of liquid impacting on the wall $\dot{q}_w$, the solidification time t_{solid} and the geometry of the incoming droplet and that of the splat:

$$N_h = \frac{3\dot{q}_w t_{solid} d_{res}^2}{2d^3}. \quad (12)$$

Roisman [22] and Van Hinsberg et al. [23] proposed expressions for the residual splat thickness. In this deposition model the residual thickness h_{res} and diameter d_{res} of liquid splat are given by:

$$h_{res} = \max\left[\min\left(0.79d\text{Re}_n^{-2/5}, \sigma_d/\tau_w\right), d\right], \quad (13)$$

and

$$d_{res} = \sqrt{\frac{2(1 - \phi_{dry})d^3}{3h_{res}}}. \quad (14)$$

In these expressions d is the diameter of the impacting droplet, Re_d the droplet Reynolds number, σ_d the surface tension and τ_w the shear stress of the air at the substrate. The shear stress is obtained from calculations of the air flow, as was described in section 5. In this study the values of h_{res} are limited to the diameter of the incoming droplet to avoid that the residual thickness becomes non-physically large.

7   Solidification

At present, still little is known about the morphological instability of a solidification front of

growing ice crystals. Li et al. [4] propose the following estimation of the drop solidification time:

$$t_{solid} \approx \frac{c^{h_{res}^2}}{T_m - T_d}, \quad \text{where} \quad c = 3 \times 10^8 \, \text{Ks}^{\text{m}^{-2}}, \tag{15}$$

where T_m is the melting temperature and T_d is the droplet temperature. Their difference presents the supercooling of the droplet. The solidification time from this empirical relation is compared to the solidification time estimated from two other solidification models:

- supercooled, planar solidification model,

- dendritic solidification model.

7.1 Planar solidification

Worster [24], among others, has derived the theory of planar solidification, which is based on the Stefan problem. Two different cases can be distinguished, see Fig. 10: planar (left) and supercooled (right). For both conditions the solidification front will have moved by a distance $h(t)$ (assuming one-dimensional heat conduction). In the planar case there will be a temperature gradient in the solid ice layer with melting temperature T_m at the liquid-ice interface and temperature T_s at the solid surface where $T_s < T_m$. In the supercooled case the solid phase is maintained at the melting temperature and the latent heat is conducted into the liquid, with the initial temperature of the liquid T_∞ below the melting temperature. The boundary conditions together with the energy equation in the solid and the conservation requirement given by the Stefan condition admit a similarity solution. Both planar and supercooled solutions are shown below Fig. 10. These two solutions are very comparable. A detailed derivation can be found in the work of Worster [24]. In Eq. (17) and Eq. (18) κ is the thermal diffusivity of the solid, t the solidification time, λ a dimensionless constant that determines the solidification rate and Ste is the Stefan number. The Stefan number is the ratio of the latent heat of solidification L and the sensible heat required to cool the newly formed solid to the surface tem-

perature and is defined as:

$$\text{Ste} = \frac{L}{C_p(T_m - T_s)}. \tag{16}$$

Here, C_p is the specific heat of the solid. If the Stefan number is large, the solidification rate λ is small. The supercooled growth rate has an asymptote at Ste = 1, but nevertheless it is possible to perform experiments for which Ste < 1. This is because for Ste > 1 the rate of solidification is controlled by the removal of latent heat, while for Ste < 1 the kinetics of molecular attachment are rate controlling [24].

7.2 Dendritic solidification

Planar solidification is (mostly) governed by diffusion. Crystal growth governed by kinetics is still poorly understood. The rate of solidification is then determined by how fast molecules are able to find a proper position in the solid structure and a small disturbance will initiate a rapid and unstable process of dendrite formation. Theoretical models based on an analytical solution for dendritic solidification had been derived, among others, by Ivantsov [25] and Langer and Muller-Krumbhaar [26]. Shibkov et al. [27] experimentally studied the pattern formation during the free growth of ice crystals in supercooled pure water in a supercooling range of [0, 30]°C. The results from their measurements are given in Fig. 11 and show that the dendritic tip velocity increases with increasing supercooling. The dendritic tip velocity is the velocity at which the solidification front (tip) of the dendrite moves into the liquid water.

In the dendritic solidification model it is assumed that dendrites are formed quickly, as is illustrated in Fig. 12b, and that the temperature of the liquid in-between the dendrites is increased to the melting temperature. The solidification rate is obtained by an empirical fit through the data of Shibkov et al. [27]. Then, in the second phase, the water in-between the dendrites solidifies, see Fig. 12c. This solidification process is initiated by the surface temperature, which is assumed to be much lower than the melting temperature. The process is planar and stable. The solidification rate is then given by Eq. 17.
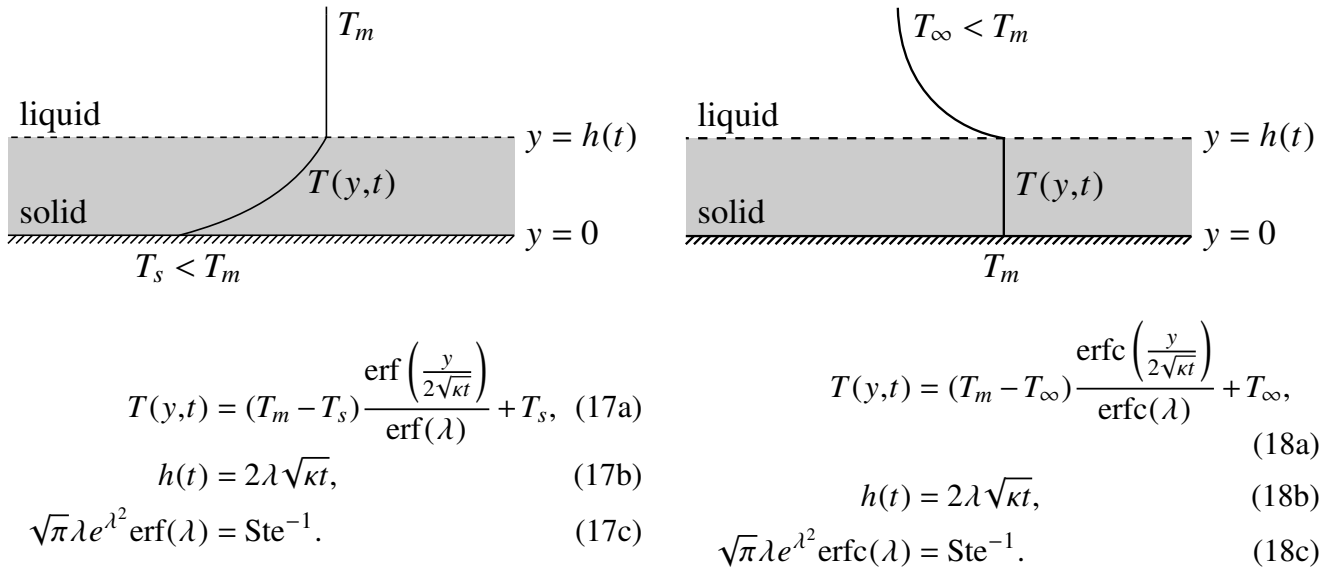
$$T(y,t) = (T_m - T_s)\frac{\text{erf}\left(\frac{y}{2\sqrt{\kappa t}}\right)}{\text{erf}(\lambda)} + T_s, \quad (17\text{a})$$

$$h(t) = 2\lambda\sqrt{\kappa t}, \quad (17\text{b})$$

$$\sqrt{\pi}\lambda e^{\lambda^2}\text{erf}(\lambda) = \text{Ste}^{-1}. \quad (17\text{c})$$

$$T(y,t) = (T_m - T_\infty)\frac{\text{erfc}\left(\frac{y}{2\sqrt{\kappa t}}\right)}{\text{erfc}(\lambda)} + T_\infty, \quad (18\text{a})$$

$$h(t) = 2\lambda\sqrt{\kappa t}, \quad (18\text{b})$$

$$\sqrt{\pi}\lambda e^{\lambda^2}\text{erfc}(\lambda) = \text{Ste}^{-1}. \quad (18\text{c})$$

Fig. 10 : Planar solidification front after some time t at normal conditions (left) and supercooled conditions (right), together with their similarity solution. Adapted from Worster [24].
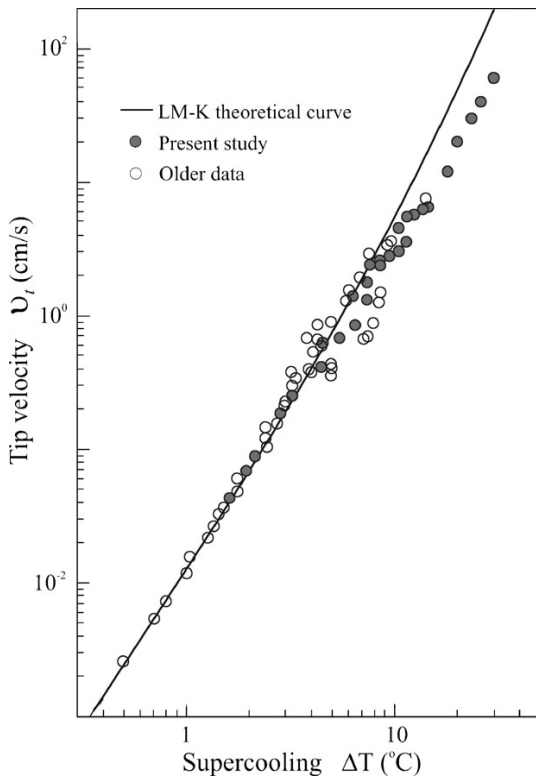
Fig. 11 : Comparison between the results of the thermal diffusion theory and experiment for growth velocity of freely growing ice crystals as a function of supercooling temperature differences, Shibkov et al. [27]
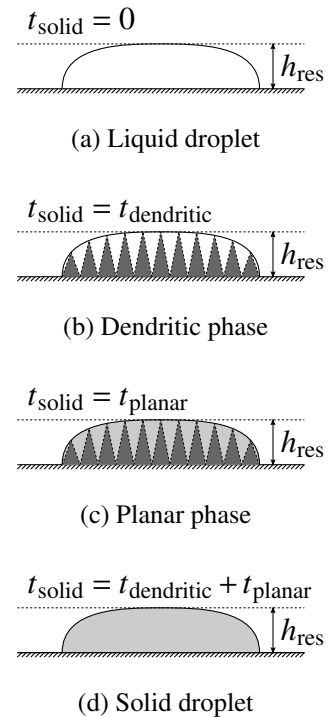
Fig. 12 : Solidification steps in combined dendritic and normal, planar solidification model.

7.3 Solidification time

Both solidification models result in a solidification rate that can be used to determine the solidification time. For the planar, supercooled solidification and the planar part of the dendritic solidification model the values of h_{res} and the Stefan number are needed. The solidification rate is then computed by a combined Newton-Raphson and secant method. For the unstable part of the dendritic solidification an empirical fit through the experimental results from Shibkov et al. gives the velocity of the solidification front. Here, only the residual thickness is needed in order to calculate the solidification time.

8 Results: Papadakis test case

In Fig. 13 the computed distribution of the catching efficiency for Papadakis test case A ($T = 299$ K) is compared with experimental results. Here 'Hospers' refers to the original splashing model in the computational method, i.e. the model of Honsek et al. [6], and 'Darmstadt' refers to the deposition model by Li et al. [4]. Because the temperature is above the freezing point, the solidification time is expected to be infinite. Since the Darmstadt model does not hold for negative freezing values of supercooling, it is assumed that the wetting parameter N_h is larger than one and thus that the mass-loss coefficient for the liquid regime is applied. The catching efficiency for the Darmstadt model is slightly lower than the catching efficiency computed by the original model over the whole region of impingement. The results of the Darmstadt model show good agreement with the experimental results, which are presented by the grey dots. However, some underprediction is still seen near the stagnation point, while the catching efficiency is somewhat overpredicted further downstream on the airfoil surface.

In Fig. 15 the results are shown for Papadakis test case B, in which the temperature is decreased to 268.15 K and the icing time is set to 600 s. Together with the results from the Hospers and Darmstadt model, the results from the models with the supercooled solidification time (planar)

and the combined dendritic and planar solidification time (dendritic) are shown. It can be observed that the results for the Darmstadt model and the planar model are almost the same. Furthermore, the results from the dendritic model match the results from Hospers closely. The latter two have a higher catching efficiency over the whole impingement range compared to the first two. This indicates that the dendritic model on the one hand, and the planar and Darmstadt model on the other, are most likely in a different deposition regime (dry or wet). The high-frequency wiggles in the region between airfoil-coordinates 0 and -0.1 are caused by the chosen grid resolution. The grid in the nose region is very fine at the surface but becomes coarser quickly with distance from the surface, see Fig. 4.

Finally, the results for the layer of accreted ice are shown in Fig. 17. The shape of the ice layer around the nose of the airfoil is similar for all four deposition models. Further downstream the ice layer extends further along the airfoil when the catching efficiency is higher. This results in the Darmstadt model having the shortest ice layer and the dendritic model having the most extended ice layer.

8.1 Solidification time

In order to analyse the solidification time for the different models the average solidification time per bin is depicted in Fig. 14. The results for Papadakis test case B ($T = 268.15$ K) discussed in the preceding section are in the left graph. The average solidification time, that is the mean solidification time of all droplets in one specific bin, is shown for the three different solidification models, together with the standard error of the mean. For the Darmstadt model the time is almost constant, while for the dendritic model the solidification time per bin is very small and increases slightly with increasing bin number or initial droplet size. The planar solidification model has a long solidification time, approaching 1 second for the first nine bins, and is approximately 4.3 seconds for bin 10 (left out of the plot for resolution reasons). The standard error is
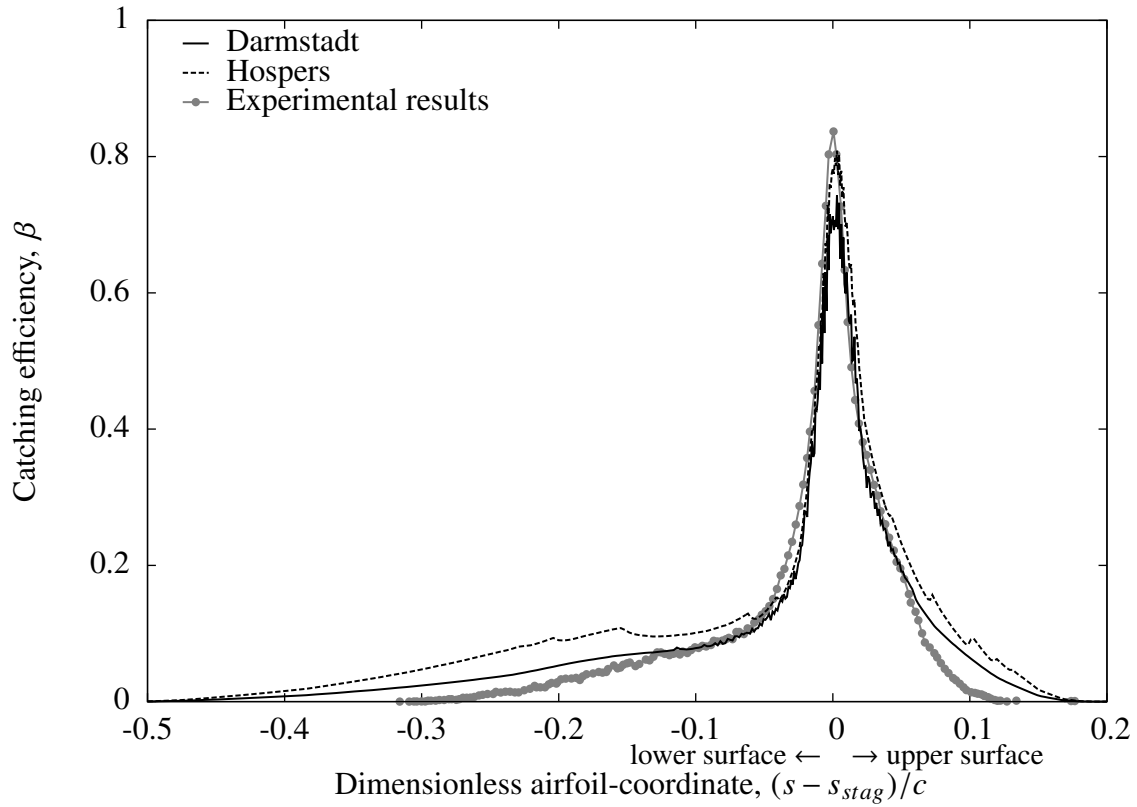
Fig. 13 : Catching efficiency for Papadakis test case A (T = 299 K) in case of SLD splashing only.
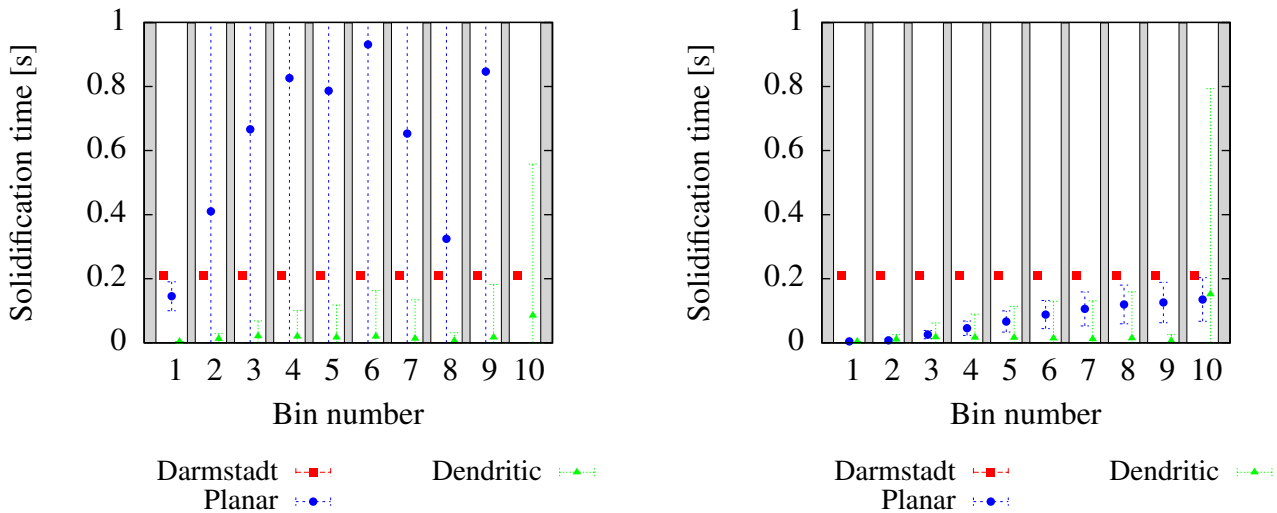

Fig. 14 : Average solidification time for SLD splashing (left) and SLD splashing and rebound (right) with standard error of the mean for Papadakis test case B (T = 268.15 K). The solidification time for bin 10 in case of planar solidification with only splashing is approximately 4.3 seconds but is left out for resolution reasons.
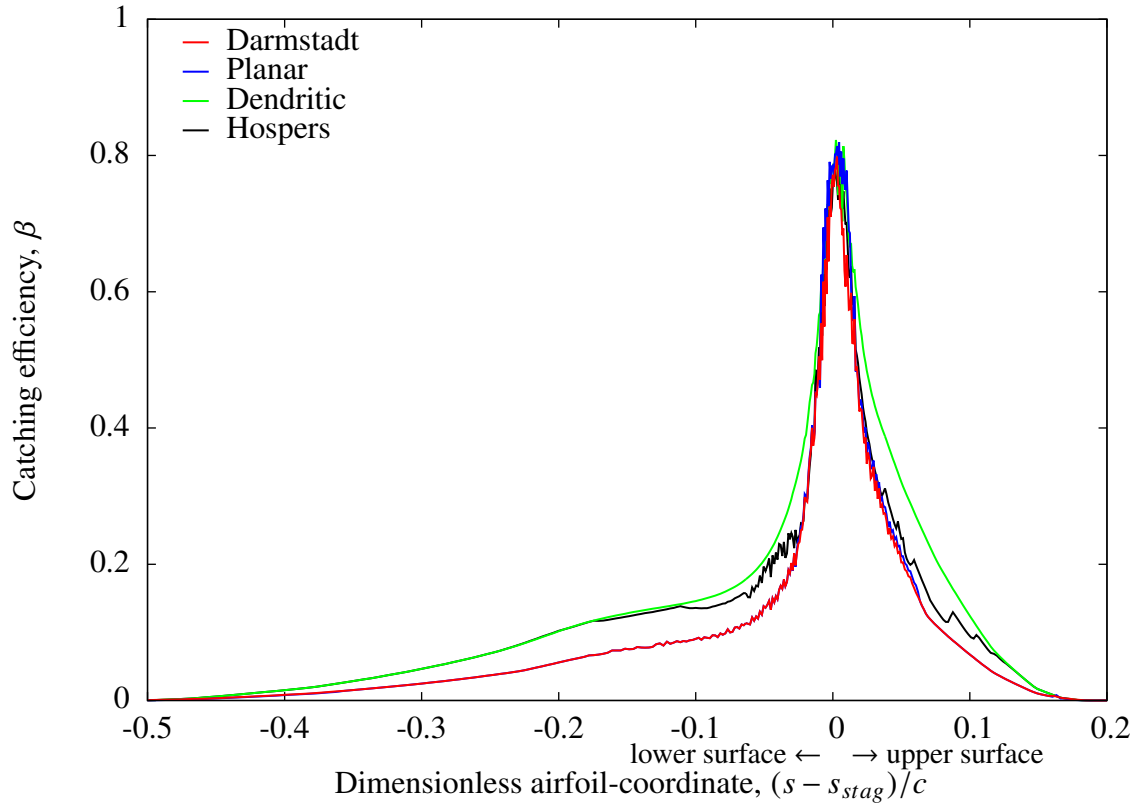
Fig. 15 : Catching efficiency for Papadakis test case B (T = 268.15 K) in case of SLD splashing only.
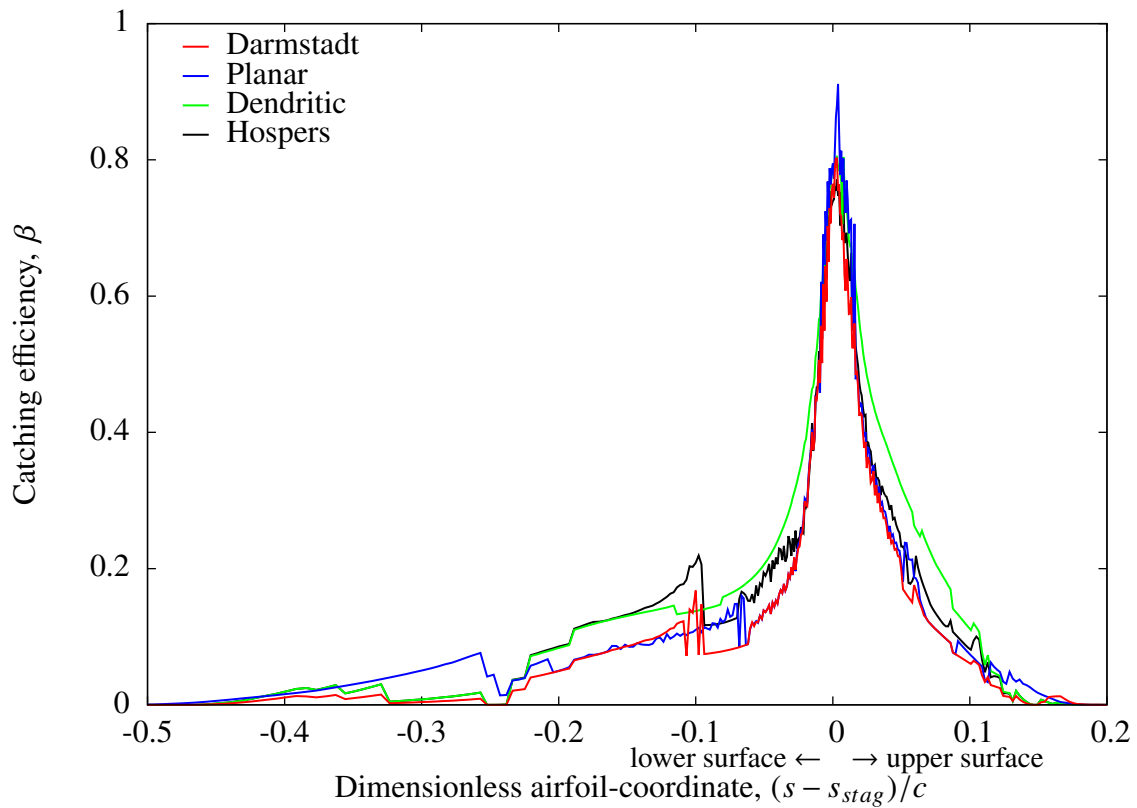
Fig. 16 : Catching efficiency for Papadakis test case B (T = 268.15 K) in case of SLD splashing and rebound.
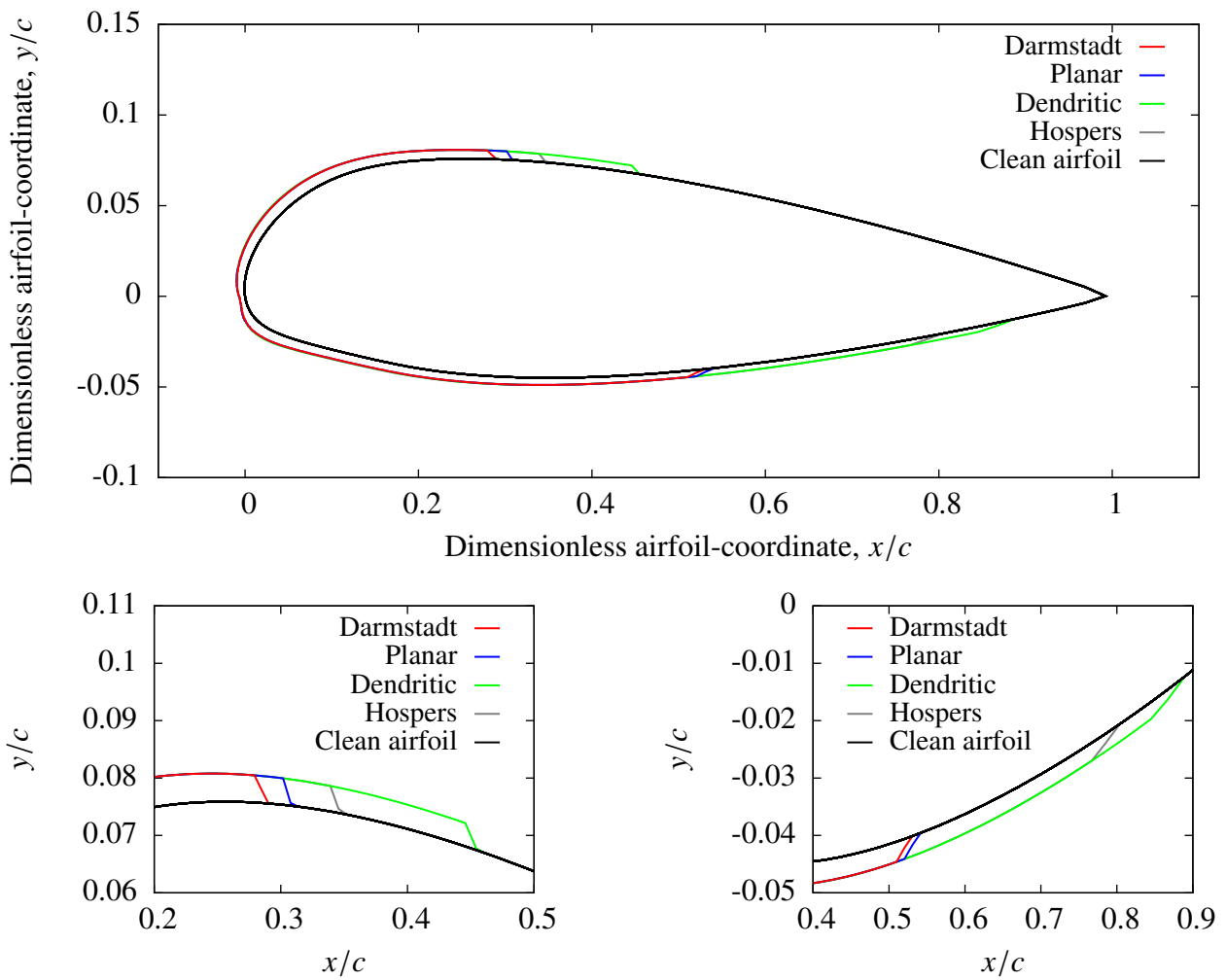
Fig. 17 : Ice accretion for Papadakis test case B (T = 268.15 K) for the complete airfoil (top) and detailed for the upper surface (lower left) and lower surface (lower right) in case of SLD splashing only.
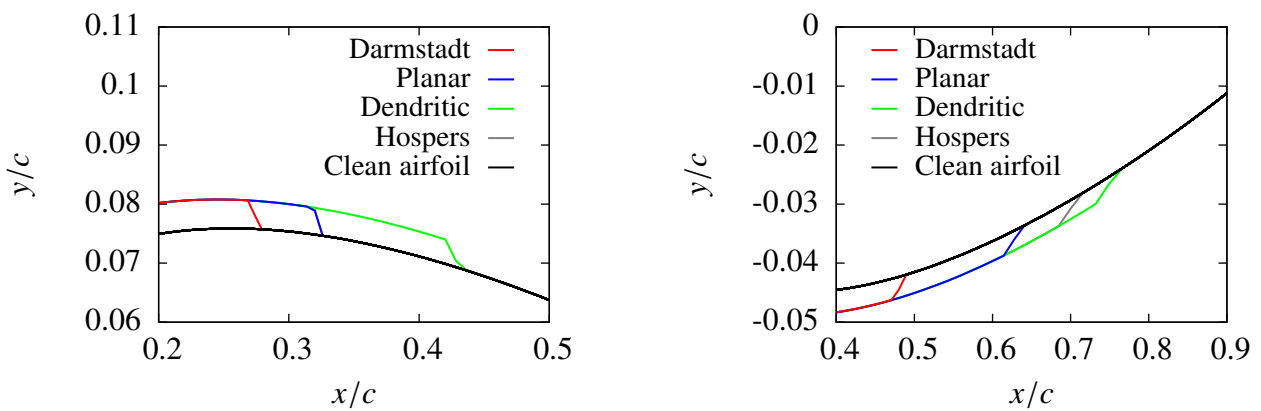

Fig. 18 : Ice accretion for Papadakis test case B (T = 268.15 K) detailed for the upper surface (left) and lower surface (right) in case of SLD splashing and rebound.

also very large. This can be explained by look-
ing at the solidification time in the right graph
in which both SLD splashing and rebound are
included. The solidification time for the Darm-
stadt and dendritic models do not change signifi-
cantly, but the solidification time for the planar
model is now much shorter with smaller standard
errors and increases with bin size. Rebound takes
place mostly near the impingement limits where
the impact angle is low. This is also the region
where high residual thicknesses lead to a long so-
lidification time in case of the planar model. So,
if rebound is taken into account, there will be no
deposit on the surface and the solidification time
in the impingement area is lowered, resulting in
a much shorter mean solidification time per bin.

In Fig. 16 and Fig. 18 the catching efficiency
and the ice layer in the region around the upper
and lower limits on the airfoil surface are shown,
respectively, with both SLD splashing and re-
bound included. The catching efficiency curve
in case of rebound shows a much more irregu-
lar shape compared to the one for the case with
splashing (Fig. 15) in the regions where rebound
occurs. Here it should be noted that the high-
frequency fluctuations in the catching efficiency
are again caused by the grid resolution. The
largest difference is seen for the planar model, as
should be expected by the results for the solid-
ification time. For the ice accretion this results
in a more extended ice layer near the impinge-
ment limits for the planar model, while the results
for the other models show slightly less ice accre-
tion when rebound is included. The results for
the current method (Hospers) on the upper sur-
face do coincide with the results for the planar
model. Near the nose region the results for the
SLD splashing and rebound model are equal to
the results for the model with just splashing in-
cluded for all cases.

9 Results: DGA test case

The catching efficiency for the DGA test case is
shown in Fig. 19 and the ice accretion results are
shown in Fig. 20. The results for the supercooled,
planar deposition model are left out, because they
are identical to the results for the dendritic depo-

sition model. This is because in both cases the
solidification time is very short and the mass-loss
coefficient for the dry regime has been applied.
This results in an ice shape that is overpredicting
the experimental result in the nose region (green
line) and which is not very different from the cur-
rent method (blue line). The results of the Darm-
stadt deposition model approach the experimen-
tal results more closely, but are still overpredict-
ing the amount of ice accreted.

10 Conclusions

The development of a liquid film on an airfoil
surface in icing conditions has been analysed to-
gether with the extension of the splashing model
for droplet impact on a thin liquid film. The
agreement of the computational method with the
experimental data from Papadakis et al. [5] and
the ones from DGA is satisfactory.

The computed water layer develops as a con-
tinuous film over the airfoil surface and reacts
strongly to changes in shear stress due to the air
flow over the water layer. The catching efficiency
computed with the Darmstadt deposition model
for Papadakis case A ($T = 299$ K) approaches the
experimental results more closely than the one
from the original deposition model. Furthermore,
decreasing the temperature from 299 K to 268 K
(Papadakis test case B) results in a liquid layer
covering a smaller area of the airfoil surface.

At freezing conditions, the ice layer com-
puted with the new deposition model covers a
smaller area of the airfoil surface when compared
to the original model. Different estimates for the
solidification time, based on planar or dendritic
solidification, also influence the extent of the ice
layer. Overprediction of the amount of ice, how-
ever, is still present.

The prediction of the solidification time of
supercooled droplets turned out to be a difficult
task. This is because the process of solidifica-
tion for supercooled water is not yet fully under-
stood. Further research could include the devel-
opment of more accurate splashing models or a
more accurate solidification model with special
attention to the residual thickness of the freez-
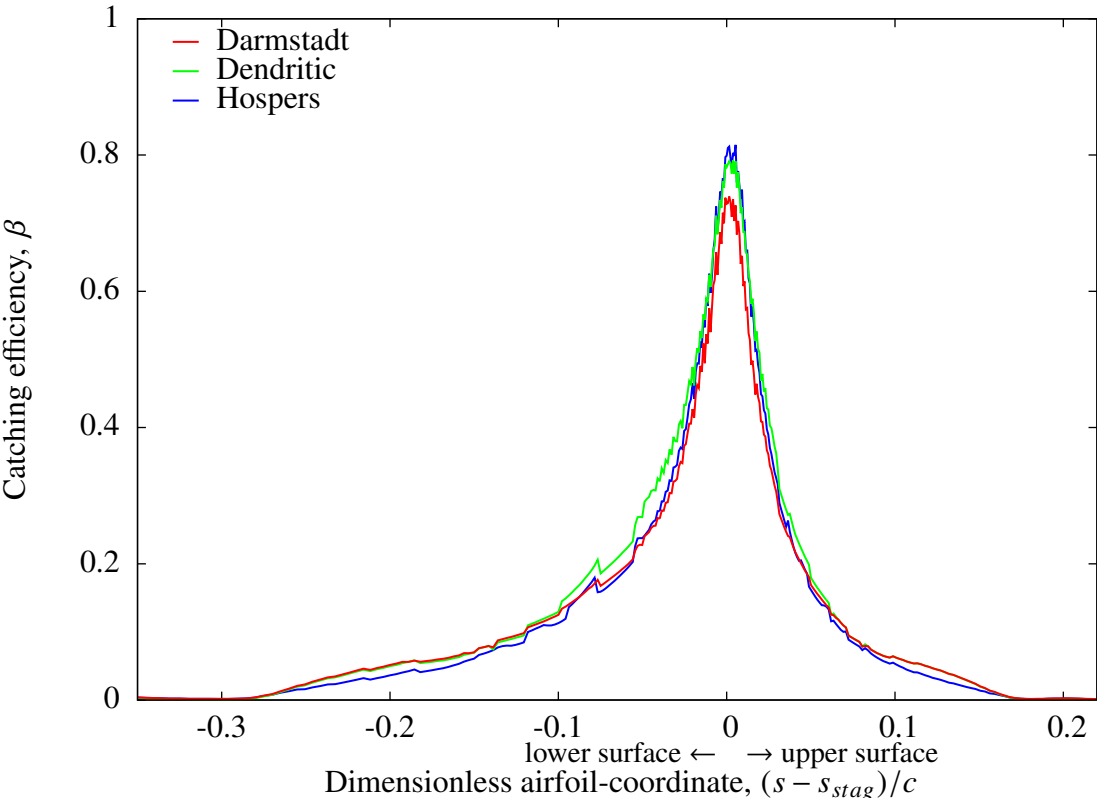ing droplet near the impingement limits. For the

Fig. 19 : Catching efficiency for the DGA test case in case of SLD splashing and rebound.
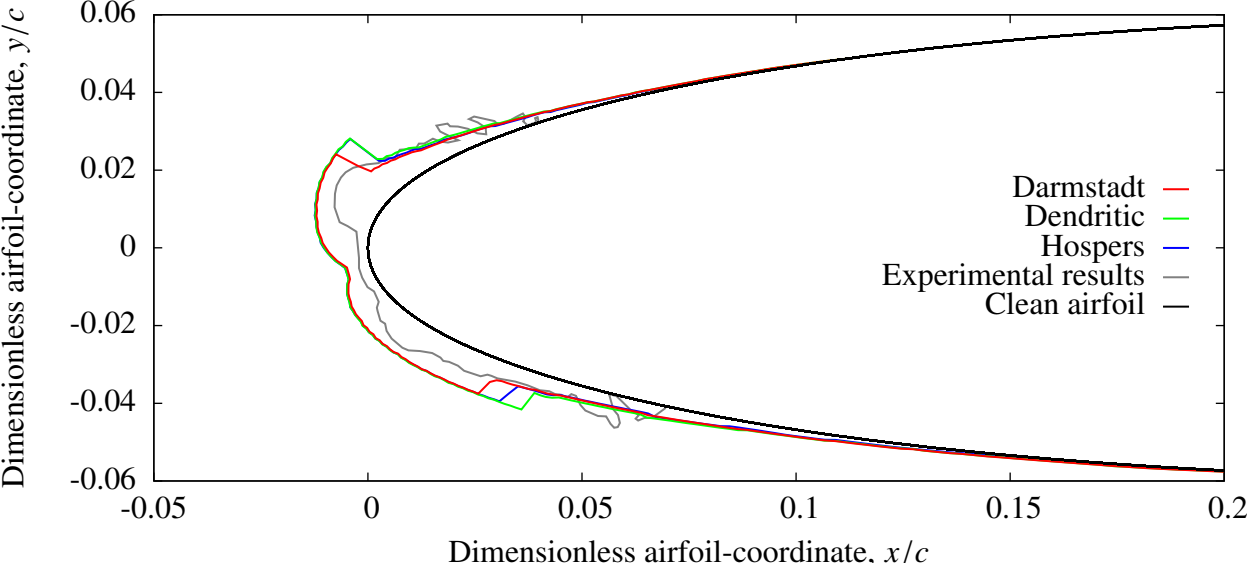

Fig. 20 : Ice accretion for the DGA test case in case of SLD splashing and rebound.

planar model this thickness has a significant effect on the solidification time and the resulting ice layer. To improve the results even further, this computational method could be extended to include the thickness of the liquid film in its deposition model. The stability of the film, now assumed as continuous, should then also be taken into account.

11 Acknowledgements

References

[1] Marwitz J., Politovich M., Bernstein B., Ralph F., Neiman P., Ashenden R. and Bresch J. Meteorological conditions associated with the ATR72 aircraft accident near Roselawn, Indiana, on 31 October 1994, *Bull. Am. Meteorolog. Soc.*, Vol. 78, No. 1, pp. 41-52, 1997.

[2] Federal Register, Airplane and engine certification requirements in supercooled large drop, mixed phase, and ice crystal icing conditions, https://federalregister.gov/a/2010-15726, 2010. Visited: June 10, 2014.

[3] Mingione G., Iuliano E., Guffond D. and Tropea C. EXTICE: EXtreme ICing Environment, *SAE International Conference on Aircraft and Engine Icing and Ground Deicing*, Chicago Illinois, SAE2011-38-0063, 2011.

[4] Li H., Roisman I.V., and Tropea C. Experiments and modelling of splash, WP2 Final Technical Report, EXTICE, 2012.

[5] Papadakis M., Rachman A., Wong S.-C., Yeong H.-W., Hung K.E., Vu G.T. and Bidwell C.S. Water droplet impingement on simulated glaze, mixed, and rime ice accretions, Technical Report NASA/TM-2007-213961, NASA Glenn Research Center, 2007.

[6] Honsek R., Habashi W.G. and Aubé, M.S. Eulerian modeling of in-flight icing due to supercooled large droplets, *J. Aircraft*, Vol. 45, No. 4, pp. 1290-1296, 2008.

[7] Trujillo M.F., Mathews W.S., Lee C.F. and Peters, J.E. Modelling and experiment of impingement and atomization of a liquid spray on a wall, *Int. J. Engine Res.*, Vol. 1, No. 1, pp.87-105, 2000.

[8] Bai C. and Gosman A.D. Development of methodology for spray impingement simulation, *SAE 2005 International Congress & Exposition*, Detroit, Michigan, SAE1995-02-0083, 1995.

[9] Hospers J.M. Eulerian method for super-cooled large-droplet ice-accretion on aircraft wings, PhD thesis, University of Twente, 2013.

[10] Hospers J.M. and Hoeijmakers H.W.M. Eulerian method for ice accretion on multiple-element airfoil sections, *48th AIAA Aerospace Sciences Meeting Including the New Horizons Forum and Aerospace Exposition*, Orlando, Florida, AIAA2010-1236, 2010.

[11] Hospers J.M. and Hoeijmakers H.W.M. Numerical simulation of SLD ice accretions, *SAE International Conference on Aircraft and Engine Icing and Ground Deicing*, Chicago, Illinois, SAE2011-38-0071, 2011.

[12] Messinger B.L. Equilibrium temperature of an unheated icing surface as a function of air speed, *J. Aeronaut. Sci.*, Vol. 20, No. 1. pp. 29-42, 1953.

[13] Jacobs S.J., Hospers J.M. and Hoeijmakers H.W.M. Numerical simulation of ice accretion on multiple-element airfoil sections, *ICAS 26th International Congress of the Aeronautical Sciences*, Anchorage, Alaska, ICAS2008-2.2.2., 2008.

[14] Tropea C. and Marengo M. Impact of drops on walls and films, *Multiphase Sci. Technol.*, Vol. 11, No. 1, pp 19-36, 1999.

[15] Wang A.-B. and Chen C.-C. Splashing impact of a single drop onto very thin liquid films, *Phys. Fluids*, Vol. 12, No. 9, pp 2155-2158, 2000.

[16] Van der Zee T.T.J. Flow over airfoil covered with thin layer of liquid, MSc thesis, University of Twente, Enschede, the Netherlands, 2008.

[17] Thwaites B. Approximate calculation of the laminar boundary layer, *Aeronaut. Quart.*, Vol. 1, pp. 245-280, 1949.

[18] Head M.R. Entrainment in the turbulent boundary layer, *Aeronautical Research Council R& M 3152*, 1958.

[19] Michel R. Étude de la transition sur les profiles d'aile; éstablissement d'un critère de determination du point de transition et calcul de la trainée de profile incompressible, ONERA rapport 1/1578A, 1951.

[20] Li H. Drop impact on dry surfaces with phase change, PhD thesis, Darmstadt University of Technology, Darmstadt, Germany, 2013.

[21] Okawa T., Shiraishi T. and Mori T. Effect of impingement angle on the outcome of single water drop impact onto a plane water surface, *Exp. Fluids* Vol. 44, pp.331-339, 2008.

[22] Roisman I.V. Inertia dominated drop collisions. II. An analytical solution for the Navier-Stokes equations for spreading viscous film, *Phys. Fluids*, Vol. 21, No. 5, pp. 052104, 2009

[23] Van Hinsberg N.P., Budakli M., Göhler S., Berberović E., Roisman I.V., Gambaryan-Roisman T., Tropea C. and Stephan P. Dynamics of the cavity and the surface film for impingements of single drops on liquid films of various thicknesses, *J. Colloid Interface Sci.*, Vol. 350, No. 1, pp. 336-343, 2010.

[24] Worster M. G. Solidification of Fluids, *Perspec. Fluid Dyn.*, Cambridge University Press, 2000.

[25] Ivantsov G.P. Temperature field around spherical, cylindrical, and needle-shaped crystals which grow in supercooled melt, *Dokl. Akad. Nauk USSR*, Vol. 58, pp. 567-569, 1947.

[26] Langer J.S. and Muller-Krumbhaar H. Theory of dendritic growth, *Acta Metall.*, Vol. 26, No. 11 pp. 1681-1687, 1978.

[27] Shibkov A.A., Golovin Y.I., Zheltov M.A., Korolev A.A. and Leonov A.A. Morphology diagram of non-equilibrium patterns of ice crystals growing in supercooled water, *Physica A*, Vol. 319, pp. 65-79, 2003.

Contact Author Email Address

Ellen Norde, mailto: e.norde@utwente.nl